ACCEPTED MANUSCRIPT • OPEN ACCESS

Hydrogen production from methane via Inductively Coupled Plasma reactor: 2D simulation of impact of input power

To cite this article before publication: Abdelatif Gadoum *et al* 2025 *Phys. Scr.* in press https://doi.org/10.1088/1402-4896/ae2551

Hydrogen Production from Methane via Inductively Coupled Plasma Reactor: 2D Simulation of Impact of Input Power

Abdelatif Gadoum[1,2] and Djilali Benyoucef[1] and Jonathan Tennyson[3,*]
gdabdelatif@gmail.com d.benyoucef@univ-chlef.dz j.tennyson@ucl.ac.uk

[1] Laboratory of Electrical Engineering and Renewable Energies, Chlef University, Chlef, Algeria
[2] Kasdi Merbah University of Ouargla, LRPPS Laboratory, Faculty of Mathematics and Material Sciences, Ouargla 30000, Algeria
[3] Department of Physics and Astronomy, University College London, London WC1E 6BT, UK

***Correspoding Author:** j.tennyson@ucl.ac.uk*

Abstract

This study presents a numerical investigation of hydrogen production from methane using an Inductively Coupled Plasma (ICP) reactor, emphasizing the influence of the imput power on plasma characteristics and methane conversion. A two dimensional fluid model was developed and solved using the finite element method, incorporating more than 300 plasma chemical reactions to capture detailed kinetics. Simulations were performed for power levels ranginf from 100W to 700W. Results show that increasing the input power significantly enhances plasma temperature from approximately 4500K to 8200K and elevate electron density from 1.2×10^{16} m^{-3} to 8.9×10^{16} m^{-3}. Consequently, methane conversion efficiency rises from 35% to about 90%, with hydrogen yield increasing by nearly 70%. These findings confirm that higher input power strengthens electron energy and collision frequency, thereby improving energy transfer and methane dissociation. The proposed modeling approach provides valuable insights for optimizing plasma assisted methane reforming and supports the development of high efficiency hydrogen production technologies.

Keywords -Inductively Coupled Plasma (ICP); Methane Reforming; Hydrogen Production; Finite Element Modeling; Plasma Chemistry; Power Dependence; Cold Plasma Reactor.

1- INTRODUCTION

Hydrogen has emerged as a crucial energy solution in the transition towards sustainability [1], offering a clean alternative to fossil fuels [2]. As a versatile energy carrier, it excels in generating electricity without polluting emissions, significantly contributing to greenhouse gas reduction [3]. However, challenges persist, including the urgent need to develop more sustainable production methods and suitable distribution infrastructure [5]. Recent advancements in green hydrogen production technologies and decarbonization initiatives promise to strengthen its integration into the global energy landscape, paving the way for a cleaner and more sustainable energy future [6-10].

Concurrently, methane, the primary constituent of natural gas [11], plays a pivotal role as a precursor for hydrogen production owing to its high hydrogen content and established extraction and distribution infrastructure [12-15]. Within the framework of global efforts towards sustainable energy

sources, methane is a versatile feedstock capable of generating hydrogen through various processes such as steam reforming [16], partial oxidation [17], and dry reforming [18]. These processes effectively exploit methane's hydrogen-rich composition and offer pathways to mitigate carbon emissions when coupled with carbon capture and utilization technologies [19-20]. This paper investigates hydrogen production via methane dissociation in an inductively coupled plasma (ICP) reactor, with the aim of contributing to the advancement of clean energy technologies and mitigation of global environmental challenges.

Inductively Coupled Plasma (ICP) reactors represent an advanced and versatile technology in the field of chemical reactions [21-23]. In ICP reactors, a high-temperature plasma is generated by inductive electric fields produced from a time-varying electromagnetic field. These electric fields accelerate electrons, resulting in collisional heating and ionization of molecular species. [24-25]. These devices offer several notable advantages, including high energy efficiency, uniform heating, and the ability to operate at atmospheric or sub-atmospheric pressures [26-27].

This study aims to explore the efficiency and feasibility of hydrogen production via plasma-assisted methane reforming, leveraging the capabilities of the reactor to enhance the reaction kinetics and yield. The main objective of this study is to predict the amount of hydrogen that could be produced.

Daghagheleh et al. [28] investigated H_2 production from methane pyrolysis by refining process parameters and analyzing their qualitative impacts. For this they used design of experiment software for statistical analysis and utilized advanced characterization techniques such as Scanning Electron Microscopy (SEM), Energy Dispersive X-ray Spectroscopy (EDS), Raman spectroscopy, X-ray diffraction (XRD) analysis and Inductively Coupled Plasma Mass Spectroscopy (ICP-MS) analysis to study solid carbon properties and confirm product purity.

Dawkins et al. [29] conducted experiments to optimize the catalytic activity through ball milling of iron ore, observing a significant increase in methane conversion to 5% after 270 minutes of milling, followed by a decrease to 4% due to particle agglomeration. Characterization techniques including Scanning Electron Microscopy (SEM), Raman spectroscopy, and Mössbauer spectra identified phase transitions in the catalyst from magnetite to maghemite and hematite with increased milling time. Analysis of the carbon byproduct highlighted its high purity, suggesting potential applications as an additive in steel production.

Abuseada et al. [30] developed a novel solar-thermal methane pyrolysis process utilizing a fibrous carbon medium to simultaneously produce hydrogen fuel and high-value graphitic carbon. Parametric studies varied methane flow rate, solar power, peak flux, operating pressure, and medium thickness, achieving methane conversions from 22% to 96%, hydrogen yields from 21% to 94%, and high-purity graphitic carbon products collected within the medium.

McConnachie et al. [31] evaluated the addition of metal sulfides to molten salt slurry systems for methane pyrolysis, conducting stability tests at 800°C in eutectic sodium and potassium bromide for 6 hours. Results show enhanced hydrogen production with metal sulfides (MoS_2) particles achieving 2.75% methane conversion at 800°C, demonstrating an apparent activation energy of 57 kJ mol^{-1}. While MoS2 exhibited good structural stability, it deactivated primarily due to coking in the melt, indicating potential to lower pyrolysis temperatures despite observed instability over extended operation.

Salakhi et al. [32] focused on hydrogen and solid carbon co-generation via microwave-driven methane pyrolysis in a fluidized bed of carbon pellets. Numerical simulations employing a coupled gas-solid chemistry approach demonstrate enhanced methane conversion, H_2 selectivity, and carbon deposition rates due to microwave thermal effects. The dominant pathway for solid carbon production was found to be C_2H_2 deposition onto carbon pellets, minimizing carbon black formation and enhancing H_2 selectivity, highlighting the effectiveness of carbon pellets in reducing the role of complex molecules like polycyclic aromatic hydrocarbons in the pyrolysis process.

Ibrahim et al. [33] explored the enhancement of methane decomposition and hydrogen production with iron catalysts for using ultrasound-assisted preparation with La_2O_3 and CeO_2 doping. Through comprehensive analyses including X-Ray Diffraction XRD, Hydrogen Temperature-Programmed oxidation Reduction (H2-TPR), H_2 chemisorption, Raman spectroscopy, Thermo-Gravimetric Analysis (TGA), and temperature-programmed oxidation (TPO), the research demonstrates that La_2O_3 doping prevents $FeAl_2O_4$ formation, enhances Fe reduction, and increases active sites on the catalyst surface. Compared to traditional methods, ultrasound-assisted catalysts show superior performance, achieving a remarkable methane conversion rate of 93% and hydrogen yield of 84% at 800°C. This innovative approach not only enhances hydrogen production efficiency but also contributes significantly to advancing sustainable energy technologies.

Scheiblehner et al. [34] explored various molten copper alloys for their effectiveness as catalytic agents in methane pyrolysis within an inductively heated bubble column reactor. Experimental results underscore the significant impact of the catalyst on methane conversion rates and the characteristics of the resulting carbon. Optimizing these factors is pivotal for enhancing the economic viability of the process.

Chen et al. [35] compared hydrogen production from one-stage (autothermal reforming of methane) and two-stage processes (partial oxidation of methane followed by water gas shift reaction) using thermodynamic analyses. They found that while the autothermal reforming temperature crucially affects hydrogen yield in the one-stage process, the two-stage process shows higher efficiency, achieving a maximum hydrogen yield of 2.89 moles of hydrogen per mole of methane at 200°C during the water gas shift reaction, indicating its superiority for hydrogen production.

Hydrogen yields of over 80% were achieved by Ahmed et al. [36] who explored methane decomposition for hydrogen production using iron-based catalysts with 20% Fe was used as the active metal part of the catalyst.

While numerous studies have investigated methane pyrolysis and reforming through various thermal, catalytic, and solar-assisted methods, there is a relative lack of detailed investigation into plasma-assisted methane dissociation—particularly using low-temperature Inductively Coupled Plasma (ICP) reactors. Existing research has largely focused on catalyst development or reactor optimization for high-temperature processes, often overlooking the complex plasma-chemical interactions and energy transfer mechanisms within ICP systems. Moreover, most studies have not systematically explored the full reaction pathways or provided predictive models of hydrogen yield based on plasma parameters.

This study aims to numerically investigate hydrogen production from methane using an Inductively Coupled Plasma (ICP) reactor, with particular emphasis on the effect of input power on hydrogen yield. Building on the previous work of Gadoum et al. [37], where methane dissociation reached approximately 90% under similar ICP conditions, this study further explores the role of power in enhancing plasma reactivity and methane decomposition efficiency. A 2D axisymmetric fluid plasma model was developed in COMSOL Multiphysics, incorporating over 300 plasma–chemical reactions to accurately represent the kinetics of methane decomposition. The model consists of four main components: a fluid model for plasma species, electromagnetic equations to determine the electric field via the magnetic vector potential, and neutral gas dynamics described by the Navier–Stokes and heat transfer equations. Together, these elements simulate weakly ionized plasma behavior under low-temperature conditions, providing deeper insight into the physical and chemical mechanisms of methane dissociation and contributing to the optimization of hydrogen production processes.

The Inductively Coupled Plasma (ICP) reactor was chosen for its stable, electrode-free plasma, ensuring minimal contamination and wide pressure operation. Its efficient energy transfer and precise power control enable effective methane dissociation and detailed analysis of plasma effects, making it ideal for optimizing methane-to-hydrogen conversion. This study explores methane dissociation and hydrogen production under varying plasma conditions.

2- MODEL DESCRIPTION

In our simulation, we employed an inductively coupled plasma (ICP) reactor configuration based on the Gaseous Electronics Conference (GEC) RF Reference Cell originally developed by Miller et al. [38]. Figure 1 illustrates the reactor geometry: a 10 mm thick quartz window separates

the plasma from the five-turn copper coil (3 mm wire diameter, 102 mm outer diameter). The stainless-steel lower electrode has a diameter of 165 mm and is positioned 40.5 mm below the quartz window, while the inner diameter of the cylindrical chamber is 251 mm. The coil is powered at a frequency of 13.56 MHz, with the central connection energized and the outer winding grounded. To ensure efficient plasma coupling, the coil is pressed firmly against the quartz plate and supported by a slotted five-arm holder mounted on top of the cell.

The oscillating current in the RF coil produces a time-varying magnetic field that induces azimuthal electric fields in the plasma via Faraday's law. These fields accelerate electrons, leading to ohmic (collisional) heating. Since no external magnetic field is applied, plasma confinement arises primarily from ambipolar electric fields and sheath potentials rather than magnetic trapping. The model represents a self-sustained inductively coupled discharge, combining a fluid description of plasma species with Maxwell's equations to determine the induced electromagnetic fields, and the Navier–Stokes equations to account for gas flow between the inlet and outlet.

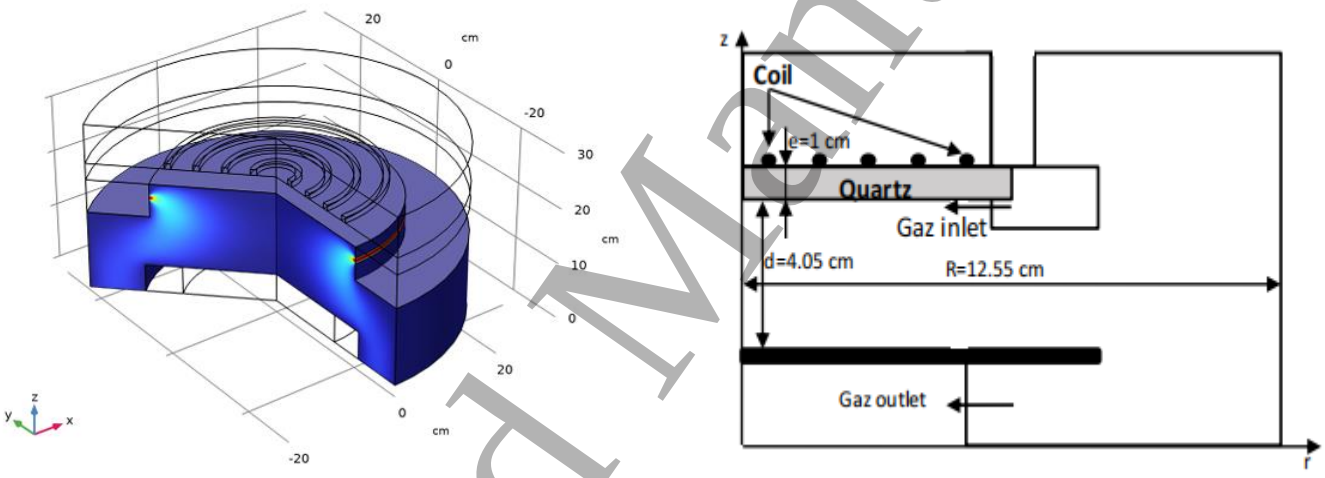

Figure1. Schematic cross-sectional diagram of the inductively coupled plasma reactor modelled in this study.

In the axisymmetric (2-D) implementation, the flat five-turn spiral coil is represented by five coaxial circular loops (rings) arranged along the axial direction, each carrying the same time-harmonic current and spaced to preserve the original radial footprint of the planar spiral. This approach follows the validated methodology described in the COMSOL Application Gallery tutorial "Model of an Argon/Chlorine Inductively Coupled Plasma Reactor with RF Bias" (Application ID 110171). To ensure accurate representation of near-field electromagnetic distributions and power-absorption characteristics, a mesh sensitivity study was conducted. Refining the mesh in the coil–plasma interface region from approximately 40,000 to 120,000 elements resulted in less than 2 % variation in both the total absorbed power and the azimuthal electric-field maxima. Consequently, the axisymmetric ring representation and adopted mesh resolution are considered sufficient to reproduce the relevant physical behavior of the actual five-turn spiral coil.

2.1. Equations of the plasma species

In fluid models, each species is modeled independently to ensure conservation of mass throughout the computational domain. Following Costin et al. [39], the electrons were assumed to conform to a Maxwellian distribution, which is generally not valid when their energy is below 15eV at low pressures. However, deviations from this distribution, particularly in the form of a high-energy tail in the electronic energy distribution function (EEDF), can lead to discrepancies between model predictions and experimental observations [40].

References [39] and [40] show that the Maxwellian assumption reasonably approximates reaction rates under similar conditions, with non-Maxwellian effects having minimal impact on overall chemistry within typical fluid modeling uncertainties.

The governing equations for electrons in these models encompass continuity, momentum, and energy equations. The model considers only continuity and momentum equations for ions. These equations are interlinked and coupled by Poisson's equation, which establishes the relationship between the space charge and the electrostatic potential within the framework of inductively coupled discharges [39].

The detailed equations used in this work are fully described in references [41-42]

In order to resolve the equations of this self-consistent fluid model, we used the following boundary conditions.

- ***Electrical potential and magnetic potential:*** The reactor walls are considered perfectly conductive and connected to the ground, this implies that the electric potential and the magnetic vector potential are zero at the metal walls, at the level of the dielectric wall, the electric potential can be obtained taking into account the following condition:

$$\frac{\partial \sigma_s}{\partial t} = n J_i + n J_e \quad (1)$$

$$-n\left(D_p - D_d\right) = \sigma_s \quad (2)$$

σ_s, n, J_i, J_e, D_p, and D_d are, respectively, the charge accumulated on the surface of the dielectric, the surface norm, the ion current density, the electronic current density, and the electric displacement vectors in the plasma side and in the dielectric side.

- ***Density, flux and energy species***: The electron flow at the walls and electrodes is obtained using the boundary condition of a Maxwellian flux where:

$$\Gamma_e = \frac{1}{4} v_{e,th} \cdot \exp\left(-\frac{\Delta\Phi}{k_B.T}\right) \quad (3)$$

Where $\Delta\Phi = \Phi_w - \Phi_p$ With: Φ_w is the wall potential and Φ_p is the plasma potential

$$v_{e,th} = \sqrt{\frac{8k_bT_e}{\pi m_e}} \quad (4)$$

where the signs ± correspond to the direction of the electron flux, V is the potential of the wall, $V_{e,th}$ is the electron thermal velocity.

Ignoring the thermal conduction of electrons, the energy flux to the electrodes and the walls is given by:

$$\Gamma_\varepsilon = \frac{5}{2} n_e T_e \Gamma_e \quad (5)$$

The ion density and velocity gradients are set to zero at the boundaries:

$$\nabla n_i = 0, \quad \nabla v_i = 0 \quad (6)$$

- **Gas flow:** the Navier-Stokes equation is solved taking into account as boundary conditions, the gas velocity at the reactor inlet, zero velocity at the walls and electrodes, and a constant pressure at the reactor outlet.

Electron mobility is calculated from their cross section and the diffusion coefficient is calculated using the Einstein relation which relates the mobility to the diffusion coefficient. The mobility of the ions is calculated using the relation of Dalgarno [43], while taking a long-range polarization interaction potential and the diffusion coefficient by the Einstein relation, which are expressed as follows:

$$\mu_i = \frac{36}{\sqrt{\alpha_n m_r}} \frac{2.69\times10^{25}}{N} \quad (7)$$

$$\frac{D_i}{\mu_i} = \frac{k_B T_i}{q_i} \quad (8)$$

where N is the gas density, q_i is the charge of the ion, μ_i is its mobility, m_r is the reduced ion-neutral mass, α_n is the polarizability in a_0^3 (where a_0 is the Bohr radius), D_i is the ionic diffusion coefficient, k_B is the Boltzmann constant, and T_i is the ionic temperature.

The diffusion coefficient of the excited particles is calculated taking into account a Lennard-Jones type interaction potential.

$$D_* = 0.0018583\sqrt{\frac{T^3}{m_r}}\ \frac{1}{p\sigma_{EN}^2\Omega_D}$$

$$\Omega_D = \frac{1.06036}{\Psi^B} + \frac{0.193}{e^{D\Psi}} + \frac{1.03587}{e^{F\Psi}} + \frac{1.76464}{e^{H\Psi}} \qquad (9)$$

$$\sigma_{EN} = \frac{\sigma_E + \sigma_N}{2},\ \ \Psi = \frac{T}{\sigma_{EN}},\ \ \varepsilon_{EN} = \sqrt{\varepsilon_E \varepsilon_N}$$

where T and p are the gas temperature and the pressure, m_r is the reduced mass, (σ_E, ε_E) *et* (σ_N, ε_N) are respectively the parameters of Leonard-Jones potential of the excited particle E and the ground state particle N. B, D,F and H are constants given by:

B= 0.15610, D= 0.47635, F = 1.52996, and *H = 3.89411*.

The reaction rate with the walls and the electrodes can be calculated as follows:

$$k_* = \frac{D_*}{\Lambda^2} \qquad (10)$$

For a reactor of radius R and height L, the effective diffusion length Λ can be expressed from the following relation [44]:

$$\Lambda^2 = \left[\left(\frac{\pi}{L}\right)^2 + \left(\frac{2.405}{R}\right)^2\right]^{-1} \qquad (11)$$

3- **Chemical model**

In this work we take into account 34 species shown as follow:

electrons (e), CH_4, C, C_2, C_2H, C_2H_2, C_2H_3, C_2H_4, C_2H_6, C_3H_8, C_4H_{10}, H_2, H, CH_3, CH_2, CH, C_2H_5, H, CH_4^+, CH_5^+, CH_3^+, CH_2^+, CH^+, C^+, C_2^+, C_2H^+, $C_2H_2^+$, $C_2H_3^+$, $C_2H_4^+$, $C_2H_5^+$, $C_2H_6^+$, H_3^+, H_2^+, H^+.

The model includes a total of 320 reactions, as documented in Tables 1 to 3 in the Appendix. Among these are 107 electron impact reactions categorized as follows: e+CH_4, e+CH_3, e+CH_2, e+CH, e+C, e+H_2, e+H, e+C_2H_6, e+C_2H_4, and e+C_2H. A detailed descriptions of electron impact cross sections for methane

used in this study are provided by our previous work [45]; we note that similar compilations are available elsewhere [46]. Electron-impact dissociation and the dissociative ionization cross sections for the other hydrocarbons species we consider are given in Table 3 of the Appendix.

Rate coefficients (see Table I) are calculated by:

$$k = A.T_g^n.exp\left(\frac{-E_a}{RT_g}\right) \quad (12)$$

In this study, wall sticking coefficients were constant, and carbon deposition was not dynamically tracked due to the short simulation timescale. Long-term soot accumulation effects on wall properties and plasma parameters will be addressed in future extended modeling.

4- Results and discussions

The simulation examines a GEC RF ICP reactor using pure methane, incorporating gas dynamics through the solution of the Navier-Stokes equation. The study maintains a consistent gas flow rate at the inlet (100 sccm) and operates at a constant gas pressure of 25 mTorr. The results presented in Figures 2-a, b and c are based on an input power deposition of 270 W in the gas phase.

The 'input power' used in this study represents the absorbed power in the plasma, obtained by integrating the ohmic power density (Re(J·E)) over the discharge volume. The RF excitation is applied to a five-turn copper coil operating at 13.56 MHz, with the center turn powered and the outer turn grounded. The coil current is prescribed in COMSOL's electromagnetic interface, and the resulting power deposition is computed self-consistently through inductive coupling. This configuration ensures accurate evaluation of the actual plasma heating rather than the nominal generator power.

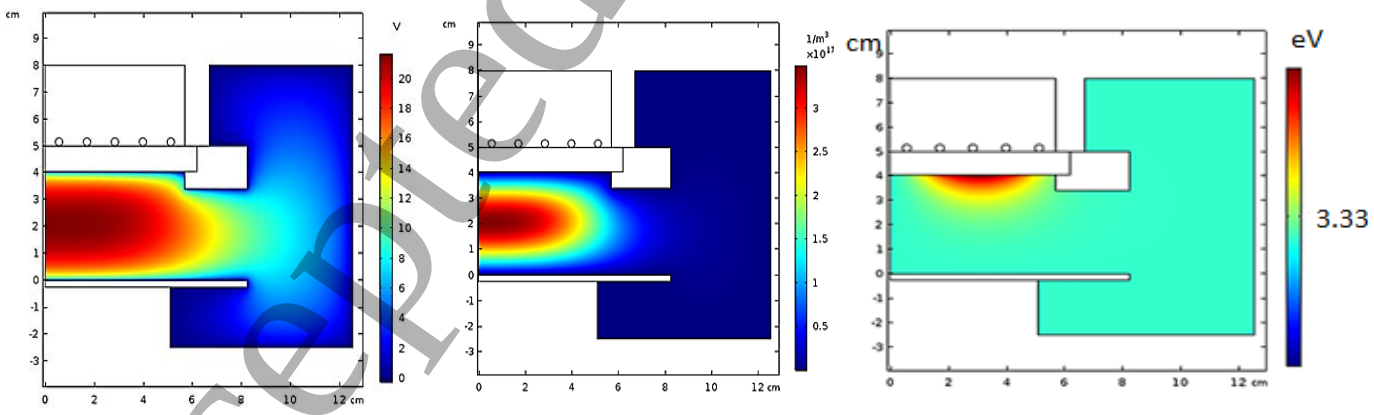

Figure 2. Results for input power 270W of Spatial variation of :

a: the electric potential, b:the electron density, and c: the electron temperature

Figure 2-a shows the spatial distribution of electric potential within the inductively coupled plasma (ICP) discharge. The electric potential remains relatively low—approximately 20 V—primarily due to space charge accumulation in the plasma region. In ICPs, electrons gain energy

predominantly from azimuthal electric fields induced by the time-varying magnetic field generated by the RF current in the coil. These induced fields drive electron heating through collisional (ohmic) mechanisms, especially near the coil, where the skin effect leads to localized energy deposition.

Figure 2-b illustrates the resulting electron density distribution, which peaks around 4×10^{12} cm^{-3} near the coil due to the efficient transfer of energy from the induced fields. Figure 2-c shows the corresponding electron temperature distribution, with elevated temperatures in regions where the induced electric fields are strongest. This spatial correlation between electric potential and electron temperature reflects how the dynamics of the induced electromagnetic field govern energy absorption and heating within the plasma.

These behaviors are characteristic of inductively coupled plasmas, where electron heating and confinement are controlled by inductive electric fields, ambipolar potentials, and sheath effects, rather than magnetic trapping. It is important to note that no static magnetic field is applied in this setup; thus, charged particle confinement does not result from magnetic mirror or magnetron-like mechanisms. Increasing the input power amplifies the strength of the induced electric field, producing more energetic electrons that collide more frequently with CH_4 molecules, thereby enhancing methane dissociation and hydrogen production.

These are common behaviors observed in this type of plasma reactor, as similarly reported in several previous studies [58-63], confirming the reliability and physical consistency of the present simulation results.

The dissociation of methane in plasma is governed by several interrelated factors, among which the input power plays a dominant role. Increasing the input power amplifies the electromagnetic field strength, producing a greater population of high-energy electrons. These electrons undergo more frequent and energetic collisions with methane molecules, leading to enhanced dissociation.

In Figure 3, our results indicate a substantial increase in methane dissociation within the inductively coupled plasma reactor as input power increases from 100 W to 700 W. However, beyond 700 W, the dissociation process is anticipated to decelerate due to reduced availability of CH_4 and diminished reactions involving methane. Conversely, the figure illustrates a significant rise in hydrogen molecules (H_2) alongside free hydrogen atoms (H).

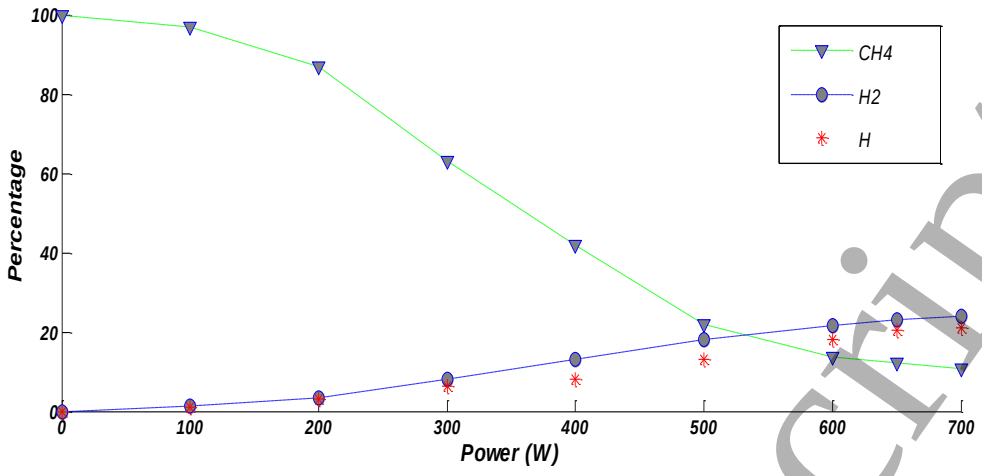

Figure 3. Variation of CH_4 dissociation, H_2 and H production as function of input power.

Figure 3 demonstrates a significant increase in methane dissociation as the input power rises from 100 W to 700 W. This enhancement is primarily driven by electron-impact reactions, where energetic electrons—heated by the azimuthal electric field induced by the RF coil—gain sufficient energy to overcome the C–H bond dissociation threshold (~4.5 eV). As input power increases, the electron temperature also rises, reaching average electron energies in the range of 4–10 eV, which are well above the energy required for bond cleavage.

Key dissociation pathways included in the model are: ($e + CH_4 \rightarrow CH_3 + H + e$ and $e + CH_4 \rightarrow CH_2 + H_2 + e$)

These reactions are part of a detailed plasma chemical mechanism incorporated into the simulation, ensuring a physically accurate representation of methane decomposition under varying plasma conditions.

The local plasma environment strongly influences dissociation rates. Space charge accumulation alters the electric field distribution, while ambipolar electric fields help confine charged species and maintain plasma quasi-neutrality. Although the time-varying magnetic field generated by the RF current is essential for inducing the heating electric field, it does not directly trap electrons or ions, as no static magnetic field is applied in this configuration.

Overall, the strong correlation observed between electron temperature, electric potential, and dissociation efficiency underscores the critical role of induced electric fields in governing energy transfer, reaction kinetics, and plasma chemistry in inductively coupled plasma discharges.

These findings highlight the importance of understanding the interplay between field strength, temperature, and particle dynamics for optimizing plasma-based methane conversion in Inductively Coupled Plasma (ICP) discharges.

Our simulation results are consistent with the findings reported in the most recent work by Alireza G. et al. [64], who observed a clear dependence of methane conversion on the input RF power. As shown in their Fig. 6(a), the methane conversion rate increases significantly with rising RF power due to enhanced energy available for ionization and dissociation processes. At higher power levels, the intensified electric field produces more energetic electrons, which collide with CH_4 molecules, leading to bond-breaking and the generation of reactive species such as CH_3, CH_2, CH, and H radicals through dissociation, vibrational excitation, and ionization. Their study reported methane conversion rates reaching 91% at 600 W, confirming the strong and rapid influence of RF power on methane cracking. This enhancement was directly attributed to the increase in plasma density and electron temperature at higher power levels, which collectively boost the overall reaction rates within the discharge region.

Thus, both our model and the experimental observations of Alireza G. et al. demonstrate a consistent trend: higher input power leads to higher electron energy, stronger dissociation rates, and consequently, greater methane conversion efficiency.

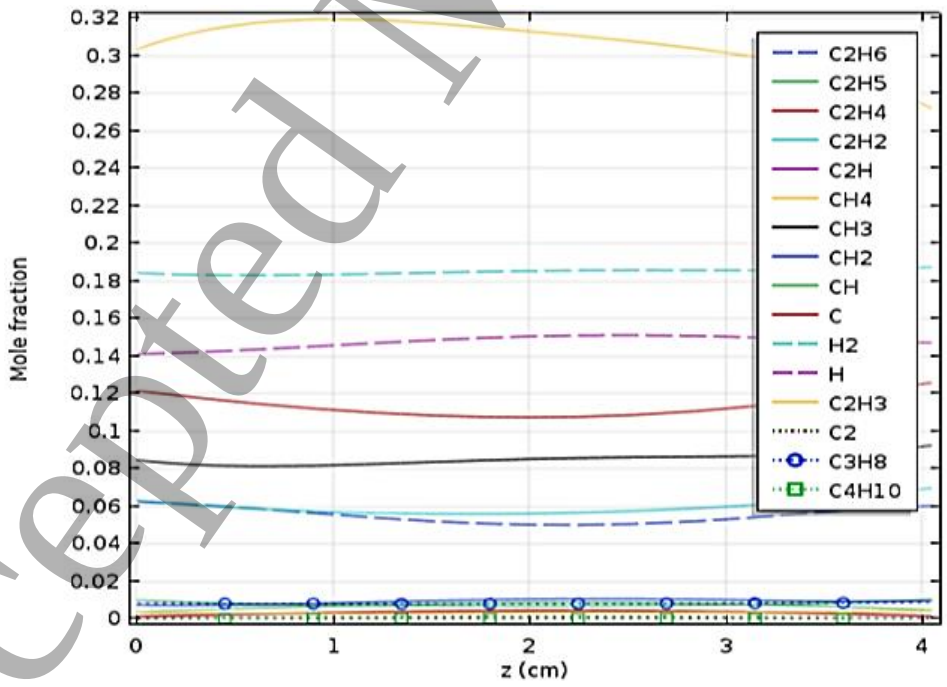

Figure 4. Mole fraction distributions of the different neutrals species at the centerof the reactor (input power of 270W).

In an inductively coupled plasma (ICP) discharge operating at 13.56 MHz, the relatively low electric potential (~20 V) observed in our simulation primarily results from space charge accumulation, which shapes the local electric field distribution. Importantly, no externally applied static magnetic field is present in this configuration. Electron heating and plasma sustainment are driven by inductive electric fields generated by the time-varying magnetic field associated with the RF coil current. These azimuthal electric fields accelerate electrons via the skin effect, leading to localized power deposition, particularly near the coil. The resulting increase in electron energy and density—reaching values around 4×10^{12} cm^{-3}—supports efficient ionization and dissociation processes. Particle confinement in this system arises from ambipolar electric fields and sheath structures near boundaries, rather than magnetic trapping. Understanding the interplay between induced electric fields, electron heating, and ambipolar confinement is essential for optimizing plasma chemistry and process performance in ICP reactors.

Moreover, higher input power enhances energy transfer to electrons and ions, increasing plasma temperature and density—key parameters for accelerating dissociation processes. While the hydrodynamic residence time of methane molecules is mainly governed by flow rate, volume, and gas density, the effective reaction time within the plasma increases with power. Stronger electric fields accelerate charged particles and raise their collision frequency with methane molecules, leading to more frequent dissociation events and higher overall conversion efficiency.

Additionally, more power leads to a denser plasma with more reactive species, which further extends the interaction time of methane molecules with these species. Increased electron temperatures at higher power levels result in more effective energy transfer during collisions, breaking molecular bonds more efficiently. The higher energy input also raises the frequency of collisions among particles, giving methane molecules a longer time in the plasma before exiting. These combined effects stronger electric fields, higher plasma density, increased energy transfer, and extended collision interactions result in a greater likelihood of methane dissociation, making the process more efficient.

The electromagnetic field's role in trapping electrons and ions is crucial in these reactors, particularly under the influence of coils, as shown in previous figures. This environment fosters multiple reactions, contributing significantly to the efficiency and effectiveness of methane dissociation processes within the plasma.

The profile density of different neutrals at the center axis of discharge (r=0) is shown in Figure4. This figure indicates that the most important species after CH_4 in these conditions is the hydrogen molecule (H_2), this molecule is created primarily by the first process in the plasma

which is the electron impact collision, these reactions are the dissociation into: CH_2+H_2, $CH+H_2+H$, and $C+2H_2$, and also through dissociative ionization of methane molecule like: $CH_2{+}{+}H_2$, $CH{+}{+}H_2+H$, and $C{+}{+}2H_2$. Other reactions also lead to increase the amount of the H_2 produced, such as $CH_4+H\rightarrow CH_3+H_2$ and $CH_3+H\rightarrow CH_2+H_2$. Although CH_3 and CH_2 are the first molecule formed in this process ($e+CH_4\rightarrow e+CH_3+H$ with threshold of 8.8 eV, $e+CH_4\rightarrow e+CH_2+H_2$ with threshold of 9.4 eV) but their reactions especially ($CH_3+CH_3\rightarrow C_2H_4+H_2$, $CH_3+CH_2\rightarrow C_2H_4+H$, $CH_2+CH_2\rightarrow C_2H_4$) effectively reduces their quantities and increases mainly the amount of C_2H_4 molecule, as shown in the Figure 4.

5- Conclusion

This work presents a comprehensive numerical investigation of methane decomposition in an inductively coupled plasma (ICP) reactor using a self-consistent fluid model. The model incorporates over 300 plasma chemical reactions and couples species transport, electromagnetic field equations, and gas flow dynamics. Plasma behavior is governed by the conservation equations for electrons and ions, along with Poisson's equation to compute the electric field distribution. Gas dynamics are accounted for via the Navier-Stokes equations, allowing for a realistic simulation of flow, pressure, and species transport within the reactor.

The results demonstrate that increasing the applied RF power significantly enhances key plasma parameters—including electron density, electron temperature, and overall energy transfer efficiency. These changes directly promote electron-impact dissociation of methane, leading to elevated production of reactive species and hydrogen. Notably, the model predicts a methane conversion rate approaching 90% at 700 W input power and a methane mole fraction of 10%, confirming the sensitivity of dissociation processes to plasma operating conditions.

Electron heating is achieved through inductive coupling, where time-varying currents in the RF coil generate azimuthal electric fields that accelerate electrons. This mechanism sustains the plasma through collisional heating, without the use of a static magnetic field. Particle confinement in this configuration arises primarily from ambipolar electric fields and sheath potentials near surfaces, not magnetic trapping.

The observed behavior is consistent with established physical principles of low-temperature ICPs. Higher power levels result in elevated electron energies and increased collision frequencies, both of which enhance the efficiency of energy transfer and methane dissociation. These processes are accompanied by a rise in the production of molecular and atomic hydrogen, highlighting the reactor's potential for hydrogen generation via plasma-assisted reforming.

Overall, the simulation confirms the strong capability of the developed fluid model to capture the key physical and chemical phenomena governing methane conversion in ICP discharges. However, experimental validation remains essential to verify these predictions and assess their applicability to real plasma systems.

Future work will aim to integrate diagnostic techniques—such as optical emission spectroscopy and mass spectrometry—to quantitatively validate species densities and conversion rates. Additional efforts will focus on extending the model to explore the effects of operating pressure, RF frequency, and reactor geometry on plasma uniformity and chemical selectivity. Incorporating surface reactions, vibrational kinetics, and more detailed chemical pathways will also be pursued to refine the model's accuracy. These improvements will support the optimization of plasma-based methane reforming for efficient hydrogen production and broader energy applications.

Data availability

The data that support the findings of this study are included within the article.

Conflict of interest

The authors declare no conflicts of interest.

APPENDIX

Table 1. Reactions with Rate coefficient.

N	Reactions	Rate Coefficient			Reference
		A[m3/s.mol]	E[J/mol]	n	
01	$CH_4 + CH_2 => CH_3 + CH_3$	0.0713E-16	41988	0	47
02	CH_4 +CH=>C_2H_4+H	153E-16		-0.9	46
03	CH_4 +H=>CH_3+H_2	2.2E-26	33632	3	45
04	$CH_3+CH_3=>C_2H_6$	4.66E-16		-0.37	47
05	$CH_3+CH_3=>C_2H_4+H_2$	170E-16	133030		46
06	$CH_3+CH_3=>C_2H_5$+H	0.5E-16	56540		47
07	$CH_3+CH_2=>C_2H_4$+H	0.7E-16			47
08	CH_3+CH=>C_2H_3+H	0.5E-16			46
09	CH_3+C=>C_2H_2+H	0.83E-16			46
10	CH_3+H2=>CH_4 +H	1.1E-26	39410	2.74	46
11	CH_3+H=>CH_2+H_2	1E-16	63190		47
12	$CH_2+CH_2=>C_2H_4$	0.017E-16			48
13	$CH_2+CH_2=>C_2H_2$+2H	1.8E-16	3326		46
14	$CH_2+CH_2=>C_2H_2+H_2$	26.3E-16	50000		46
15	$CH_2+CH_2=>CH_3$+CH	4E-16	41572		46
16	CH2+CH=>C_2H_2+H	0.66E-16			48
17	CH_2+C=>C_2H+H	0.83E-16			48
18	$CH_2+H_2=>CH_3$+H	0.19E-16	53212	0.17	46
19	CH_2+H=>CH+H_2	2.2E-16			46
20	CH+CH=>C_2H_2	2E-16			47
21	CH+C=>C_2+H	0.66E-16			46
22	CH+H_2=>CH_2+H	5.46E-16	16055		46
23	CH+H=>C+H_2	1.31E-16	665		47
24	C+H_2=>CH+H	6.64E-16	97278		47
25	CH_4++CH_4=>CH_5^++CH_3	11.5E-16			49
26	CH_4^++H2=>CH_5^++H	1.086E-16	-300	-0.14	46
27	CH_4^++H=>CH_3^++H2	0.1E-16			46
28	CH_5^++CH_2=>CH_3^++CH_4	9.6E-16			46
29	CH_5^++CH=>CH_2^++CH_4	120E-16		-0.5	46

30	CH_5^++C=>CH^++CH_4	12E-16			46
31	CH_5^++H=>CH_4^++H_2	1.5E-16			46
32	CH_3^++CH_4=>$C_2H_5^+$+H_2	9.6E-16			49
33	CH_3^++CH_2=>$C_2H_3^+$+H_2	9.9E-16			46
34	CH_3^++CH=>$C_2H_2^+$+H_2	123E-16		-0.5	46
35	CH_3^++C=>C_2H^++H_2	12E-16			46
36	CH_3^++H=>CH_2^++H_2	7E-16	87800		46
37	CH_2^++CH_4=>$C_2H_5^+$+H	2.88E-16			46
38	CH_2^++CH_4=>$C_2H_4^+$+H_2	5E-16			46
39	CH_2^++CH_4=>$C_2H_3^+$+H_2+H	2.64E-16			46
40	CH_2^++CH_4=>$C_2H_2^+$+2H_2	1.44E-16			46
41	CH_2^++C=>C_2H^++H	12E-16			46
42	CH_2^++H_2=>CH_3^++H	7.2E-16			49
43	CH_2^++H=>CH^++H_2	10E-16	58866		46
44	CH^++CH_4=>$C_2H_4^+$+H	0.77E-16			46
45	CH^++CH_4=>$C_2H_3^+$+H_2	10.57E-16			46
46	CH^++CH_4=>$C_2H_2^+$+H_2+H	1.55E-16			46
47	CH^++CH_2=>C_2H^++H_2	10E-16			46
48	CH^++CH=>C_2^++H_2	128E-16		-0.5	46
49	CH^++C=>C_2++H	12E-16			46
50	CH^++H_2=>CH_2^++H	10.1E-16			46
51	CH^++H=>C^++H_2	74.75E-16	241	-0.37	46
52	C^++CH_4=>$C_2H_3^+$+H	10.3E-16			46
53	C^++CH_4=>$C_2H_2^+$+H_2	4.2E-16			46
54	C^++CH_3=>$C_2H_2^+$+H	13E-16			46
55	C^++CH_3=>C_2H^++H_2	10E-16			46
56	C^++CH_2=>C_2H^++H	5.2E-16			46
57	C^++CH_2=>CH_2^++C	5.2E-16			46
58	C^++CH=>C_2^++H	65.8E-16		-0.5	46
59	C^++CH=>CH^++C	65.8E-16		-0.5	46
60	C^++H2=>CH^++H	1E-16	38579		46
61	H_3^++CH_4=>CH_5^++H_2	10.3E-16			46
62	H_3^++CH_4=>CH_3^++2H_2	10.3E-16			46

63	$H_3^+ + CH_3 => CH_4^+ + H_2$	21E-16			46
64	$H_3^+ + CH_2 => CH_3^+ + H_2$	17E-16			46
65	$H_3^+ + CH => CH_2^+ + H_2$	207E-16		-0.5	46
66	$H_3^+ + C => CH^+ + H$	20E-16			46
67	$H_2^+ + CH_4 => CH_4^+ + H_2$	14E-16			46
68	$H_2^+ + CH_4 => CH_5^+ + H$	1.1E-16			46
69	$H_2^+ + CH_4 => CH_3^+ + H_2 + H$	22.8E-16			46
70	$H_2^+ + CH_2 => CH_2^+ + H_2$	10E-16			46
71	$H_2^+ + CH_2 => CH_3^+ + H$	10E-16			46
72	$H_2^+ + CH => CH^+ + CH_2$	123E-16		-0.5	46
73	$H_2^+ + CH => CH_2^+ + H$	123E-16		-0.5	46
74	$H_2^+ + C => CH^+ + H$	24E-16			46
75	$H_2^+ + H_2 => H_3^+ + H$	21E-16			46
76	$H_2^+ + H => H^+ + H_2$	6.4E-16			46
77	$H^+ + CH_4 => CH_4^+ + H$	15.2E-16			46
78	$H^+ + CH_4 => CH_3^+ + H_2$	22.8E-16			46
79	$H^+ + CH_3 => CH_3^+ + H$	34E-16			46
80	$H^+ + CH_2 => CH_2^+ + H$	14E-16			46
81	$H^+ + CH_2 => CH^+ + H_2$	14E-16			46
82	$H^+ + CH => CH^+ + H$	329E-16		-0.5	46
83	$C_2H_4^+ + H => C_2H_3^+ + H2$	3E-16			46
84	$CH_4 + C_2H_3 => C_2H_4 + CH_3$	2.41E-30	22860	4.02	47
85	$CH_4 + C_2H => C_2H_2 + CH_3$	0.03E-16	2079	0	47
86	$CH_3 + C_2H_6 => C_2H_5 + CH_4$	0.9E-30	34670	4	47
87	$CH_3 + C_2H_5 => C_3H_8$	8.11E-16		-0.5	47
88	$CH_3 + C_2H_5 => C_2H_4 + CH_4$	0.019E-16			47
89	$CH_3 + C_2H_3 => C_2H_2 + CH_4$	8833E-16	2494	-1.5	46
90	$CH_2 + C_2H_3 => C_2H_2 + CH_3$	0.3E-16			45
91	$CH_2 + C_2H => C_2H_2 + CH$	0.3E-16			45
92	$CH + C_2H_6 => C_2H_4 + CH_3$	4.8E-16	242.7	-0.52	46
93	$H_2 + C_2H => C_2H_2 + H$	3.9203e-25	1081	2.57	46
94	$H + C_2H_5 => + C_2H_6$	0.6E-16			48
95	$H + C_2H_5 => CH_3 + CH_3$	0.6E-16			50

96	H+C_2H_5=>C_2H_4+H_2	0.03E-16			50
97	H+C_2H_4=>C_2H_5	0.14E-20	4150	1.49	47
98	H+C_2H_4=>C_2H_3+H_2	2.2E-24	51220	2.53	46
99	H+C_2H_3=>C_2H_2+H_2	0.332E-16			46
100	H+C_2H_2=>C_2H +H_2	3.8E-16	113359		46
101	C_2H_6+C_2H =>C_2H_5 + C_2H_2	0.067E-16	-515	0.28	45
102	C_2H_5 + C_2H_5=>C_2H_6+C_2H_4	0.024E-16			47
103	C_2H_5+C_2H_5=>C_4H_{10}	0.19E-16			47
104	C_2H_5+C_2H =>C_2H_4+C_2H_2	0.03E-16			47
105	CH_4^++C_2H_6=>$C_2H_4^+$+CH_4 + H_2	19.1E-16			49
106	CH_4^++C_2H_4=>$C_2H_4^+$+CH_4	13.8E-16			46
107	CH_4^++C_2H_4=>$C_2H_5^+$+CH_3	4.23E-16			46
108	CH_4^++C_2H_2=>$C_2H_2^+$+CH_4	11.3E-16			46
109	CH_4^++C_2H_2=>$C_2H_3^+$+CH_3	12.3E-16			46
110	CH_5^++C_2H_4=>$C_2H_5^+$+CH_4	15E-16			46
111	CH_5^++C_2H_2=>$C_2H_3^+$+CH_4	16E-16			46
112	CH_5^++C_2H =>$C_2H_2^+$+CH_4	9E-16			46
113	CH_5^++C2=>C_2H^++CH_4	9.5E-16			46
114	CH_3^++C_2H_6=>$C_2H_5^+$+CH_4	14.8E-16			46
115	CH_3^++C_2H_4=>$C_2H_3^+$+CH_4	3.5E-16			46
116	CH_3^++C_2H_3=>$C_2H_3^+$+CH_3	51.9E-16		-0.5	46
117	C^++C_2H_6=>$C_2H_5^+$+CH	2.31E-16			46
118	C^++C_2H_6=>$C_2H_4^+$+CH_2	1.16E-16			46
119	C^++C_2H_6=>$C_2H_3^+$+CH_3	4.95E-16			46
120	C^++C_2H_6=>$C_2H_2^+$+CH_4	0.825E-16			46
121	C^++C_2H_5=>$C_2H_5^+$+C	5E-16			46
122	C^++C_2H_4=>$C_2H_4^+$+C	0.17E-16			46
123	C^++C_2H_4=>$C_2H_3^+$+CH	0.85E-16			46
124	H_3^++C_2H_6=>$C_2H_5^+$+2H_2	34E-16			49
125	$H_3^{++C_2H_5}$=>$C_2H_6^+$+H_2	14E-16			46
126	H_3^++C_2H_4=>$C_2H_5^+$+H_2	14.4E-16			46
127	H_3^++C_2H_4=>$C_2H_3^+$+2H_2	21.6E-16			46
128	H_3^++C_2H_3=>$C_2H_4^+$+H_2	346E-16		-0.5	46

129	$H_3^+ + C_2H_2 \Rightarrow C_2H_3^+ + H_2$	35E-16			46
130	$H_3^+ + C_2H \Rightarrow C_2H_2^+ + H_2$	17E-16			46
131	$H_3^+ + C_2 \Rightarrow C_2H^+ + H_2$	18E-16			46
132	$H_2^+ + C_2H_6 \Rightarrow C_2H_6^+ + H_2$	2.94E-16			46
133	$H_2^+ + C_2H_6 \Rightarrow C_2H_5^+ + H_2 + H$	13.7E-16			46
134	$H_2^+ + C_2H_6 \Rightarrow C_2H_4^+ + 2H_2$	23.5E-16			46
135	$H_2^+ + C_2H_6 \Rightarrow C_2H_3^+ + 2H_2 + H$	6.86E-16			45
136	$H_2^+ + C_2H_6 \Rightarrow C_2H_2^+ + 3H_2$	1.96E-16			45
137	$H_2^+ + C_2H_4 \Rightarrow C_2H_4^+ + H_2$	22.1E-16			46
138	$H_2^+ + C_2H_4 \Rightarrow C_2H_3^+ + H_2 + H$	18.1E-16			46
139	$H_2^+ + C_2H_4 \Rightarrow C_2H_2^+ + 2H_2$	8.8E-16			46
140	$H_2^+ + C_2H_2 \Rightarrow C_2H_2^+ + H_2$	48.2E-16			46
141	$H_2^+ + C_2H_2 \Rightarrow C_2H_3^+ + H$	4.8E-16			46
142	$H_2^+ + C_2H \Rightarrow C_2H^+ + H_2$	10E-16			46
143	$H_2^+ + C_2H \Rightarrow C_2H_2^+ + H$	10E-16			46
144	$H_2^+ + C_2 \Rightarrow C_2^+ + H_2$	11E-16			46
145	$H_2^+ + C_2 \Rightarrow C_2H^+ + H$	11E-16			46
146	$H^+ + C_2H_6 \Rightarrow C_2H_4^+ + H_2 + H$	14E-16			46
147	$H^+ + C_2H_6 \Rightarrow C_2H_3^+ + 2H_2$	28E-16			46
148	$H^+ + C_2H_5 \Rightarrow C_2H_4^+ + H_2$	16.5E-16			46
149	$H^+ + C_2H_5 \Rightarrow C_2H_3^+ + H_2 + H$	30.6E-16			46
150	$H^+ + C_2H_4 \Rightarrow C_2H_3^+ + H_2$	30E-16			46
151	$H^+ + C_2H_4 \Rightarrow C_2H_2^+ + H_2 + H$	10E-16			46
152	$H^+ + C_2H_4 \Rightarrow C_2H_4^+ + H$	10E-16			46
153	$H^+ + C_2H_3 \Rightarrow C_2H_3^+ + H$	346E-16		-0.5	46
154	$H^+ + C_2H_3 \Rightarrow C_2H_2^+ + H_2$	346E-16		-0.5	46
155	$H^+ + C_2H_2 \Rightarrow C_2H_2^+ + H$	5.4E-16			46
156	$H^+ + C_2H \Rightarrow C_2H^+ + H$	15E-16			46
157	$H^+ + C_2H \Rightarrow C_2^+ + H_2$	15E-16			46
158	$H^+ + C_2 \Rightarrow C_2^+ + H$	31E-16			46
159	$C_2H_5^+ + H \Rightarrow C_2H_4^+ + H_2$	0.1E-16			46
160	$C_2H_4^+ + C_2H_3 \Rightarrow C_2H_5^+ + C_2H_2$	86.6E-16		-0.5	46
161	$C_2H_4^+ + C_2H_3 \Rightarrow C_2H_3^+ + C_2H_4$	86.6E-16		-0.5	46

162	$C_2H_3^+ + C_2H_6 => C_2H_5^+ + C_2H_4$	2.91E-16			46
163	$C_2H_3^+ + C_2H_4 => C_2H_5^+ + C_2H_2$	9.3E-16			49
164	$C_2H_3^+ + C_2H_3 => C_2H_5^+ + C_2H$	86.6E-16		-0.5	46
165	$C_2H_3^+ + C_2H => C_2H_2^+ + C_2H_2$	86.6E-16		-0.5	46
166	$C_2H_3^+ + H => C_2H_2^+ + H_2$	0.68E-16			46
167	$C_2H_2^+ + C_2H_6 => C_2H_4^+ + C_2H_4$	2.62E-16			46
168	$C_2H_2^+ + C_2H_6 => C_2H_5^+ + C_2H_3$	1.31E-16			46
169	$C_2H_2^+ + C_2H_4 => C_2H_4^+ + C_2H_2$	4.0E-16			46
170	$C_2H_2^+ + C_2H_3 => C_2H_3^+ + C_2H_2$	57E-16		-0.5	46
171	$C_2H_2^+ + H_2 => C_2H_3^+ + H$	10E-16			46
172	$C_2H^{++CH_4} => C_2H_2^+ + CH3$	3.74E-16			46
173	$C_2H^+ + CH_2 => CH_3^+ + C2$	4.4E-16			46
174	$C_2H^+ + H_2 => C_2H_2^+ + H$	7.8E-16			49
175	$C_2^+ + CH => CH^+ + C_2$	55.4E-16		-0.5	46
176	$C_2^+ + CH_4 => C_2H_2^+ + CH_2$	1.82E-16			46
177	$C_2^+ + CH_4 => C_2H^+ + CH_3$	2.38E-16			46
178	$C_2^+ + CH_2 => CH_2{+}{+} + C_2$	4.5E-16			46
179	$C_2^+ + C => C^+ + C_2$	1.1E-16			46
180	$C_2^+ + H_2 => C_2H^+ + H$	11E-16			46
181	$C_2H_6^+ + C_2H_6 => C_3H_8^+ + CH_4$	0.08E-16			45
182	$C_2H_6^+ + C_2H_4 => C_2H_4^+ + C_2H_6$	11.5E-16			46
183	$C_2H_6^+ + C_2H_2 => C_2H_5^+ + C_2H_3$	2.22E-16			51
184	$C_2H_6^+ + H => C_2H_5^+ + H_2$	1E-16			46

Table 2. Wall reactions with sticking coefficient [54].

N	Wall reaction	Sticking coefficient
01	CH_2	0.026
02	CH_3	0.001
03	CH_4	0.01
04	C_2H	0.8
05	C_2H_3	0.3
06	C_2H_5	0.01
07	H	0.07
08	C	1
09	C_2	1

Table 3. Electronic impact reactions with threshold energy (CH_4, CH_3, CH_2, CH, C, H, H_2, C_2H_2, C_2H_4, and C_2H_6) [55-57]

N	reactions	Threshold (eV)
01	$e+CH_4 \Rightarrow e+CH_3+H$	8.8
02	$e+CH_4 \Rightarrow e+CH_2+H_2$	9.4
03	$e+CH_4 \Rightarrow e+CH+H_2+H$	12.5
04	$e+CH_4 \Rightarrow e+C+2H_2$	14
05	$e+CH_4 \Rightarrow 2e+CH_4^+$	12.63
06	$e+CH_4 \Rightarrow 2e+H+CH_3^+$	14.25
07	$e+CH_4 \Rightarrow 2e+H2+CH_2^+$	15.1
08	$e+CH_4 \Rightarrow 2e+H+H_2+CH^+$	19.9
09	$e+CH_4 \Rightarrow 2e+2H_2+C^+$	19.6
10	$e+CH_4 \Rightarrow 2e+CH_2+H_2^+$	20.1
11	$e+CH_4 \Rightarrow 2e+CH_3+H^+$	18
12	$e+CH_3 \Rightarrow e+CH_2+H$	6.9
13	$e+ CH_3 \Rightarrow e+CH+H_2$	7.2
14	$e+ CH_3 \Rightarrow e+CH+2H$	12.4
15	$e+ CH_3 \Rightarrow e+C+H_2+H$	10.6
16	$e+ CH_3 \Rightarrow 2e+CH_3^+$	9.84
17	$e+ CH_3 \Rightarrow 2e+CH_2^++H$	15.12
18	$e+ CH_3 \Rightarrow 2e+CH^++H_2$	15.74

19	e+ CH_3=>2e+H^++CH_2	18.42
20	e+ CH_3=>2e+C++H+H_2	19.50
21	e+ CH_3=>2e+H2++CH	20.18
22	e+CH_2=>e+CH+H	6.4
23	e+CH_2=>e+C+H_2	6.6
24	e+CH_2=>e+C+2H	10.4
25	e+CH_2=>2e+CH_2^+	10.4
26	e+CH_2=>2e+CH^++H	15.53
27	e+CH_2=>2e+C^++H_2	14.67
28	e+CH_2=>2e+H^++CH	18.01
29	e+CH_2=>2e+H_2^++C	18.83
30	e+CH=>e+C+H	5.3
31	e+CH=>2e+CH+	10.64
32	e+CH=>2e+C^++H	14.74
33	e+CH=>2e+H^++C	17.07
34	e+C=>2e+C^+	11.26
35	e+H=>2e+H^+	13.6
36	e+H2=>e+H+H	15.0
37	e+H2=>e+H+H	16.6
38	e+H_2=>2e+H_2^+	15.4
39	e+H_2=>2e+H+H^+	18.1
40	e+C_2H_2=>e+C_2H+H	7.5
41	e+C_2H_2=>e+C_2+H_2	8.7
42	e+C_2H_2=>e+C_2+2H	11.38
43	e+C_2H_2=>e+CH+CH	10.6
44	e+C_2H_2=>e+CH_2+C	9.8
45	e+C_2H_2=>2e+$C_2H_2^+$	11.4
46	e+C_2H_2=>2e+C_2H^++H	16.48
47	e+C_2H_2=>2e+C_2^++H_2	16.76
48	e+C_2H_2=>2e+CH^++CH	20.61
49	e+C_2H_2=>2e+C^++CH_2	20.35
50	e+C_2H_2=>2e+H^++C_2H	18.46
51	e+C_2H_4=>e+C_2H_3+H	6.9
52	e+C_2H_4=>e+C_2H_2+H_2	5.8

53	$e+C_2H_4 \Rightarrow e+C_2H_2+2H$	6.5
54	$e+ C_2H_4 \Rightarrow e+C_2H+H_2+H$	8.4
55	$e+ C_2H_4 \Rightarrow e+CH_3+CH$	8.7
56	$e+ C_2H_4 \Rightarrow e+CH_2+CH_2$	8.9
57	$e+ C_2H_4 \Rightarrow e+C+CH_4$	8.1
58	$e+ C_2H_4 \Rightarrow 2e+C_2H_4^+$	11.51
59	$e+ C_2H_4 \Rightarrow 2e+C_2H_3^++H$	13.09
60	$e+ C_2H_4 \Rightarrow 2e+C_2H_2^++H_2$	13.23
61	$e+ C_2H_4 \Rightarrow 2e+C_2H^++H_2+H$	19.06
62	$e+ C_2H_4 \Rightarrow 2e+C_2^++2H_2$	20.09
63	$e+ C_2H_4 \Rightarrow 2e+CH_3^++CH$	16.91
64	$e+ C_2H_4 \Rightarrow 2e+CH_2^++CH_2$	17.94
65	$e+ C_2H_4 \Rightarrow 2e+CH^++CH_3$	18.2
66	$e+C_2H_4 \Rightarrow 2e+C^++CH_4$	18.94
67	$e+ C_2H_6 \Rightarrow e+C_2H_5+H$	7.45
68	$e+C_2H_6 \Rightarrow e+C_2H_4+H_2$	4.0
69	$e+ C_2H_6 \Rightarrow e+C_2H_3+H_2+H$	9.4
70	$e+ C_2H_6 \Rightarrow e+C_2H_2+2H_2$	6.2
71	$e+C_2H_6 \Rightarrow e+CH_4+CH_2$	6.95
72	$e+C_2H_6 \Rightarrow e+CH_3+CH_3$	6.38
73	$e+C_2H_6 \Rightarrow 2e+C_2H_6^+$	11.52
74	$e+C_2H_6 \Rightarrow 2e+C_2H_5^++H$	12.50
75	$e+C_2H_6 \Rightarrow 2e+C_2H_4^++H_2$	11.43
76	$e+C_2H_6 \Rightarrow 2e+C_2H_3^++H_2+H$	14.51
77	$e+C_2H_6 \Rightarrow 2e+C_2H_2^++2H_2$	14.65
78	$e+C_2H_6 \Rightarrow 2e+C_2H^++2H_2+H$	17.73
79	$e+C_2H_6 \Rightarrow 2e+C_2^++3H_2$	21.01
80	$e+C_2H_6 \Rightarrow 2e+CH_3^++CH_3$	13.51
81	$e+C_2H_6 \Rightarrow 2e+CH_2^++CH_4$	16.05
82	$e+C_2H_6 \Rightarrow 2e+CH^++CH_4+H$	19.1
83	$e+C_2H_6 \Rightarrow 2e+C^++CH_4+H_2$	18.77

REFERENCES

[1] Santana, Julio Ariel Dueñas, et al. Towards sustainable hydrogen production: An integrated approach for Sustainability, Complexity, and Systems Thinking in the energy sector. *Journal of Cleaner Production* 449 (2024): 141751.

[2] Laimon, Mohamd, and Talal Yusaf. Towards energy freedom: Exploring sustainable solutions for energy independence and self-sufficiency using integrated renewable energy-driven hydrogen system. *Renewable Energy* 222 (2024): 119948.

[3] Swadi, Mahmood, et al. Investigating and predicting the role of photovoltaic, wind, and hydrogen energies in sustainable global energy evolution. *Global Energy Interconnection* 7.4 (2024): 429-445.

[4] Chelvam, K., Hanafiah, M. M., Woon, K. S., & Al Ali, K. (2024). A review on the environmental performance of various hydrogen production technologies: An approach towards hydrogen economy. *Energy Reports*, 11, 369-383.

[5] Mair, Georg W., et al. Safety criteria for the transport of hydrogen in permanently mounted composite pressure vessels. International *Journal of Hydrogen Energy* 46.23 (2021): 12577-12593.

[6] Saadat, Zahra, MahgolFarazmand, and Mohammad Sameti. Integration of underground green hydrogen storage in hybrid energy generation. *Fuel* 371 (2024): 131899.

[7] Teoh, Yew Heng, et al. A review on production and implementation of hydrogen as a green fuel in internal combustion engines. *Fuel* 333 (2023): 126525.

[8] Temiz, Mert, et al. More efficient way of clean hydrogen production: The synergetic roles of magnetic effects and effective catalysts. *Fuel* 376 (2024): 132708.

[9] Lin, Ning, Yayun Chen, and Maria P. Madariaga. Route-to-market strategy for low-carbon hydrogen from natural gas in the Permian Basin. *Fuel* 355 (2024): 129420.

[10] Okoro, Victor, Ulugbek Azimov, and Jose Munoz. Recent advances in production of bioenergy carrying molecules, microbial fuels, and fuel design-a review. *Fuel* 316 (2022): 123330.

[11] Howarth, Robert W., Renee Santoro, and Anthony Ingraffea. Methane and the greenhouse-gas footprint of natural gas from shale formations: A letter. *Climatic change* 106 (2011): 679-690.

[12] Syred, Nicholas, et al. Effect of inlet and outlet configurations on blow-off and flashback with premixed combustion for methane and a high hydrogen content fuel in a generic swirl burner. *Applied energy* 116 (2014): 288-296.

[13] B. Balasubramanian, A. Lopez Ortiz, S. Kaytakoglu, D.P. Harrison, Hydrogen from methane in a single-step process. *Chemical Engineering Science* 54 (1999): 3543-3552.

[14] Abbas, Hazzim F., and WMA Wan Daud. Hydrogen production by methane decomposition: A review. *International journal of hydrogen energy* 35.3 (2010): 1160-1190.

[15] Makaryan, Iren A., et al. A comprehensive review on the prospects of using hydrogen–methane blends: challenges and opportunities. *Energies* 15.6 (2022): 2265.

[16] Franchi, Giovanni, et al. Hydrogen production via steam reforming: a critical analysis of MR and RMM technologies. *Membranes* 10.1 (2020): 10.

[17] Osman, Ahmed I. Catalytic hydrogen production from methane partial oxidation: mechanism and kinetic study. *Chemical Engineering & Technology* 43.4 (2020): 641-648.

[18] de Medeiros, Fábio Gonçalves Macêdo, Francisco Wendell Bezerra Lopes, and Bruna Rego de Vasconcelos. Prospects and technical challenges in hydrogen production through dry reforming of methane. *Catalysts* 12.4 (2022): 363.

[19] Makaryan, Iren A., et al. A comprehensive review on the prospects of using hydrogen–methane blends: challenges and opportunities. *Energies* 15.6 (2022): 2265.

[20] Sarkar, Omprakash, et al. Waste-derived renewable hydrogen and methane: towards a potential energy transition solution. *Fermentation* 9.4 (2023): 368.

[21] Dolbec, R., et al. Nanopowders synthesis at industrial-scale production using the inductively-coupled plasma technology. *International Conference on Advanced Nanomaterials & Emerging Engineering Technologies. IEEE*, 2013.

[22] Guo, Jianming, et al. Optimizing Plasma Etching: Integrating Precise Three-Dimensional Etching Simulation and Machine Learning for Multi-Objective Optimization. *IEEE Access* (2024).

[23] Shin, Hyunduck, et al. Enhanced catalytic activity and stability of SOFC electrodes through plasma-driven surface modification. *Journal of Materials Chemistry* A 12.18 (2024): 10695-10703.

[24] Zhang, W., A. Lani, and M. Panesi. Analysis of non-equilibrium phenomena in inductively coupled plasma generators. *Physics of Plasmas* 23.7 (2016).

[25] Pham, Phuong V. et al. Layer-by-layer thinning of two-dimensional materials. *Chemical Society Reviews* 53 (2024) 5190-5226.

[26] Osipov, A. A., Iankevich, G. A., Speshilova, A. B., Osipov, A. A., Endiiarova, E. V., Berezenko, V. I., ... & Alexandrov, S. E. (2020). High-temperature etching of SiC in SF_6/O_2 inductively coupled plasma. *Scientific reports*, 10(1), 19977.

[27] Y Zhao, X Zhou, S Gao, S Song and Y Zhao. (2024). Effect of coil and chamber structure on plasma radial uniformity in radio frequency inductively coupled plasma. *Plasma Science and Technology*, 26(7), 075402.

[28] Oday Daghagheleh, Johannes Schenk, Heng Zheng, Michael Andreas Zarl, Manuel Farkas, Daniel Ernst, Lina Kieush, Markus Lehner, Nikolaos Kostoglou, Robert Obenaus-emler, (2024) Optimizing methane plasma pyrolysis for instant hydrogen and high-quality carbon production", *International Journal of Hydrogen Energy*, 79, 1406-1417.

[29] Dawkins, M., Saal, D., Marco, J. F., Reynolds, J., & Dann, S. (2023). An iron ore-based catalyst for producing hydrogen and metallurgical carbon via catalytic methane pyrolysis for decarbonisation of the steel industry. *international journal of hydrogen energy*, 48(57), 21765-21777.

[30] Abuseada, M., Spearrin, R. M., & Fisher, T. S. (2023). Influence of process parameters on direct solar-thermal hydrogen and graphite production via methane pyrolysis. *International Journal of Hydrogen Energy*, 48(78), 30323-30338.

[31] McConnachie, M., Sheil, A., Konarova, M., & Smart, S. (2024). Evaluation of heterogeneous metal-sulfide molten salt slurry systems for hydrogen production through methane pyrolysis. *International Journal of Hydrogen Energy*, 49, 981-991.

[32] Salakhi, M., Cepeda, F., & Thomson, M. J. (2024). A comprehensive kinetic study on low-GHG hydrogen production from microwave-driven methane pyrolysis. *International Journal of Hydrogen Energy*, 77, 997-1008.

[33] Ibrahim, A. A., Ahmed, H., Fakeeha, A. H., Abasaeed, A. E., Al-Fatesh, A. S., & Osman, A. I. (2024). Iron catalysts enhanced by ultrasound for methane decomposition and hydrogen generation. *International Journal of Hydrogen Energy*.

[34] Scheiblehner, D., Neuschitzer, D., Wibner, S., Sprung, A., & Antrekowitsch, H. (2023). Hydrogen production by methane pyrolysis in molten binary copper alloys. *International Journal of Hydrogen Energy*, 48(16), 6233-6243.

[35] Chen, W. H., Lin, M. R., Lu, J. J., Chao, Y., & Leu, T. S. (2010). Thermodynamic analysis of hydrogen production from methane via autothermal reforming and partial oxidation followed by water gas shift reaction. I*nternational Journal of Hydrogen Energy*, 35(21), 11787-11797.

[36] Ahmed, H., Alotibi, M. F., Fakeeha, A. H., Ibrahim, A. A., Abasaeed, A. E., Osman, A. I., ... & Al-Fatesh, A. S. (2024). Hydrogen Production via Methane Decomposition over Alumina Doped with Titanium Oxide-Supported Iron Catalyst for Various Calcination Temperatures. *ChemistryOpen*, 13(4), e202300173.

[37] Gadoum, A., Tebani, H., & Benyoucef, D. (2025). *Effect of Increasing Input Power on Methane Dissociation Dynamics in Inductively Coupled Plasma Reactor: A 2-D Simulation*. IEEE Transactions on Plasma Science.

[38] Miller, P. A., Hebner, G. A., Greenberg, K. E., Pochan, P. D., & Aragon, B. P. (1995). An inductively coupled plasma source for the gaseous electronics conference RF reference cell. *Journal of research of the National Institute of Standards and Technology*, 100(4), 427.

[39] Costin, C., Marques, L., Popa, G., & Gousset, G. (2005). Two-dimensional fluid approach to the DC magnetron discharge. Plasma Sources Science and Technology, 14, 168.

[40] Jaworski, M. A., Bell, M. G., Gray, T. K., Kaita, R., Kallman, J., Kugel, H. W., ... & Surla, V. (2012). Modification of the electron energy distribution function during lithium experiments on the National Spherical Torus Experiment. Fusion Engineering and Design, 87(10), 1711-1718.

[41] https://www.comsol.com/model/gec-icp-reactor-argon-chemistry-8649

[42] H. Tebani and D. Benyoucee. A global model for the inductively coupled rf discharges in Ar/H_2 mixture. *Przegląd Elektrotechniczny* 1, 32-38 (2021).

[43] Smirnov, B. M. (1967). Diffusion and Mobility of Ions in a Gas. *Soviet Physics Uspekhi*, *10*(3), 313.

[44] S. Ramo, J. R. Whinnery, and T. Van Duzer, *Fields and Waves in Communication Electronics*, 3rd ed., Wiley, 1994.

[45] Gadoum, A., & Benyoucef, D. (2018). Set of the electron collision cross sections for methane molecule. *IEEE Transactions on Plasma Science*, 47(3), 1505-1513.

[46] M.-Y. Song, J.S. Yoon, H. Cho, Y. Itikawa, G. Karwasz, V. Kokoouline, Y. Nakamura and J. Tennyson, Cross sections for electron collisions with methane, J. Phys. Chem. Ref. Data, 44, 023101 (2015).

[47] V. Wakelam, J.-C. Loison, E. Herbst, B. Pavone, A. Bergeat, K. Beroff, M. Chabot, A. Faure, W.D. Geppert, D. Gerlich, P. Gratier, N. Harada, K.M. Hickson, P. Honvault, S.J. Klippenstein, S. Le Picard, G. Nyman, M. Ruaud, S. Schlemmer, I.R. Sims, D. Talbi, J.Tennyson and R. Wester The 2014 KIDA network for interstellar chemistry, *Astrophys. J. Suppl.*, 217, 20 (2015). http://kida.obs.u-bordeaux1.fr/search.html

[48] T. J. Millar, C. Walsh, M. Van de Sande and A. J. Markwick, The UMIST Database for Astrochemistry 2022, Astron. Astrophys. 682 (2024) A109 http://udfa.ajmarkwick.net/index.php

[49] J. A. Manion, R. E. Huie, R. D. Levin, D. R. Burgess Jr., V. L. Orkin, W. Tsang, W. S. McGivern, J. W. Hudgens, V. D. Knyazev, D. B. Atkinson, E. Chai, A. M. Tereza, C.-Y. Lin, T. C. Allison, W. G. Mallard, F. Westley, J. T. Herron, R. F. Hampson, and D. H. Frizzell, NIST Chemical Kinetics Database, NIST Standard Reference Database 17, Version 7.0 (Web Version), Release 1.6.8, Data version 2015.09, National Institute of Standards and Technology, Gaithersburg, Maryland, 20899-8320. https://kinetics.nist.gov/

[50] Mao, M., & Bogaerts, A. (2010). Investigating the plasma chemistry for the synthesis of carbon nanotubes/nanofibres in an inductively coupled plasma enhanced CVD system: the effect of different gas mixtures. *Journal of Physics D: Applied Physics*, 43(20), 205201.

[51] Huntress Jr, W. T. (1977). Laboratory studies of bimolecular reactions of positive ions in interstellar clouds, in comets, and in planetary atmospheres of reducing composition. Astrophysical *Journal Supplement Series*, vol. 33, Apr. 1977, p. 495-514., 33, 495-514.

[52] Jaritz, M., Hopmann, C., Behm, H., Kirchheim, D., Wilski, S., Grochla, D., ... & Dahlmann, R. (2017). Influence of residual stress on the adhesion and surface morphology of PECVD-coated polypropylene. *Journal of Physics D: Applied Physics*, 50(44), 445301.

[54] Huang, C. Y., Liang, M. W., Chang, C. H., Lee, K. F., & Wang, C. C. (2009). Simulation study of a capacitively coupled plasma by two dimensional fluid model. In 2009 *IEEE International Conference on Plasma Science-Abstracts* (pp. 1-1). IEEE.

[54] Mao, M., & Bogaerts, A. (2010). Investigating the plasma chemistry for the synthesis of carbon nanotubes/nanofibres in an inductively coupled plasma enhanced CVD system: the effect of different gas mixtures. *Journal of Physics D: Applied Physics*, 43(20), 205201.

[55] Janev, R. K., and D. Reiter. Collision processes of CH y and CH y+ hydrocarbons with plasma electrons and protons. Physics of Plasmas 9.9 (2002): 4071-4081.

[56] Janev, R. K., and D. Reiter. Collision processes of $C_{2,3}H_y$ and $C_{2,3}H_y^+$ hydrocarbons with electrons and protons. Physics of Plasmas 11.2 (2004): 780-829.

[57] Janev, Ratko K., and Detlev Reiter. Collision processes of hydrocarbon species in hydrogen plasmas: II. The ethane and propane families. Forschungszentrum, Zentralbibliothek, 2002.

[58] Siari, K., Rebiai, S., Bahouh, H., & Bouanaka, F. (2020). Plasma-enhanced chemical vapor deposition of silicon films at low pressure in gec reference cell. Plasma Physics Reports, 46(6), 667-674.

[59] Marza, H. H., & Khalaf, T. H. (2022). The Effect of Power on Inductively Coupled Plasma Parameters. Iraqi Journal of Physics, 20(3), 98-108.

[60] Kropotkin, A. N., & Voloshin, D. G. (2020). ICP argon discharge simulation: The role of ion inertia and additional RF bias. Physics of Plasmas, 27(5).

[61] Cheng, J., Ji, L., Wang, K., Han, C., & Shi, Y. (2013). Two-dimensional simulation of inductively coupled plasma based on COMSOL and comparison with experimental data. Journal of Semiconductors, 34(6), 066004.

[62] Chang, B., Bayat, M., Jansen, H., Hattel, J. H., & Han, A. Comparison of Radio Frequency Source Designs in Inductively Coupled Plasma Systems: A Numerical Study. Available at SSRN 4863413.

[63] Marza, H. H., & Khalaf, T. H. (2022). The Effect of Power on Inductively Coupled Plasma Parameters. Iraqi Journal of Physics, 20(3), 98-108.

[64] Ganjovi, A., Bartali, R., Speranza, G., Dell'Anna, R., Gottardi, G., Missale, E., & Laidani, N. (2025). Method for hydrogen production by methane cracking using vacuum plasma. Surface and Coatings Technology, 132393.